Matthew J. Emes, Maziar Arjomandi, Farzin Ghanadi, Richard M. Kelso

Effect of turbulence characteristics in the atmospheric surface layer on the peak wind loads on heliostats in stow position

Solar Energy, 2017; 157:284-297

Final publication at http://dx.doi.org/10.1016/j.solener.2017.08.031

Effect of turbulence characteristics in the atmospheric surface layer on the peak wind loads on heliostats in stow position

Matthew J. Emes*, Maziar Arjomandi, Farzin Ghanadi and Richard M. Kelso

School of Mechanical Engineering, The University of Adelaide, SA 5005, Australia

Abstract

This study investigates the dependence of peak wind load coefficients on a heliostat in stow position on turbulence characteristics in the atmospheric surface layer, such that the design wind loads, and thus the size and cost of heliostats, can be further optimised. Wind tunnel experiments were carried out to measure wind loads and pressure distributions on a heliostat in stow position exposed to gusty wind conditions in a simulated part-depth atmospheric boundary layer (ABL). Force measurements on different-sized heliostat mirrors at a range of heights found that both peak lift and hinge moment coefficients, which are at least 10 times their mean coefficients, could be optimised by stowing the heliostat at a height equal to or less than half that of the mirror facet chord length. Peak lift and hinge moment coefficients increased linearly and approximately doubled in magnitude as the turbulence intensity increased from 10% to 13% and as the ratio of integral length scale to mirror chord length L_u^x/c increased from 5 to 10, compared to a 25% increase with a 40% increase in freestream Reynolds number. Pressure distributions on the stowed heliostat showed the presence of a high-pressure region near the leading edge of the heliostat mirror that corresponds to the peak power spectra of the fluctuating pressures at low frequencies of around 2.4 Hz. These high pressures caused by the break-up of large vortices at the leading edge are most likely responsible for the peak hinge moment coefficients and the resonance-induced deflections and stresses that can lead to structural failure during high-wind events.

Keywords: Heliostat; Stow position; Wind load; Atmospheric surface layer

Nomenclature

A	Heliostat mirror area (m^2)
α	Power law roughness exponent
b	Spire base width (m)
c	Heliostat mirror chord length (m)
c_L	Peak lift coefficient
$c_{M_{Hy}}$	Peak hinge moment coefficient
c_P	Pressure coefficient
D	Drag force on heliostat in stow position (N)
d	Spire base depth in flow direction (m)
δ	ABL thickness (m)
f	Frequency of velocity/pressure fluctuations (Hz)
H	Elevation axis height of stowed heliostat mirror above the ground (m)
h	Spire height (m)
I_u	Turbulence intensity (%)
L_u^x	Longitudinal integral length scale (m)
L	Lift force on the flat plate (N)
$L_{heliostat}$	Lift force on the heliostat assembly with pylon and plate (N)
L_{pylon}	Lift force on the heliostat pylon without the plate (N)
l_p	Distance to the centre of pressure in the flow direction (m)
M_{Hy}	Hinge moment on heliostat in stow position (N·m)
M_y	Overturning moment on heliostat in stow position (N·m)
P_i^f	Pressure fluctuations on the upper surface of the stowed heliostat mirror (Pa)
P_i^b	Pressure fluctuations on the lower surface of the stowed heliostat mirror (Pa)
Re_∞	Freestream Reynolds number $Re_\infty = U_\infty \delta / \nu$
S_p	Power spectrum of pressure fluctuations (Pa^2/Hz)
S_u	Power spectrum of streamwise velocity fluctuations (m^2/s^3)
σ_u	Standard deviation of streamwise velocity fluctuations (m^2/s^3)
T_u^x	Longitudinal integral time scale (s)
U_∞	Freestream velocity (m/s)
$\overline{U}$	Mean velocity (m/s)
u	Streamwise velocity fluctuations (m/s)
x	Longitudinal direction (m)
y	Spanwise direction (m)
z	Height above the ground (m)

1. Introduction

The concentrating solar thermal (CST) power tower (PT) is one of the most promising renewable technologies for large-scale electricity production with thermal energy storage, and it can be deployed as a hybrid system with existing fossil fuel power plants for a base-line power supply (Hinkley et al., 2013). The main limitation of PT systems is their significantly larger levelised cost of electricity (LCOE) relative to base-load energy systems (IRENA, 2013). To reduce the LCOE of PT systems there is a need to lower the capital cost of a PT plant, of which the largest cost is the heliostat field, with an estimated contribution of between 40% and 50% (Coventry and Pye, 2014; Hinkley et al., 2013; IRENA, 2015; Kolb et al., 2007). One opportunity to lower the heliostat cost is through optimisation of the size and position of heliostat mirrors to withstand maximum wind loads during high-wind conditions when in the stow position, aligned parallel to the ground ($\alpha = 0°$). The motor drives, support structure and mirror must all withstand any forces and moments, shown in Fig. 1(a), applied to the heliostat from the wind. These components, which are identified in Fig. 1(b), account for up to 80% of the heliostat capital cost according to research by Kolb et al. (2011). A cost analysis of quasi-static wind loads on individual heliostat components by Emes et al. (2015) found that the sensitivity of the total heliostat cost to the stow design wind speed increased by 34% for an increase in mean wind speed from 10 m/s to 15 m/s. Following the linear cost-load proportionality developed by McMaster Carr, a 40% reduction in the peak hinge moment on the elevation drive of a conventional heliostat can lead to a 24% saving in the representative gear reducer cost (Lovegrove and Stein, 2012). Hence, there is significant potential to minimise the capital cost of a PT plant through optimising the structural design of heliostats in the stow position.

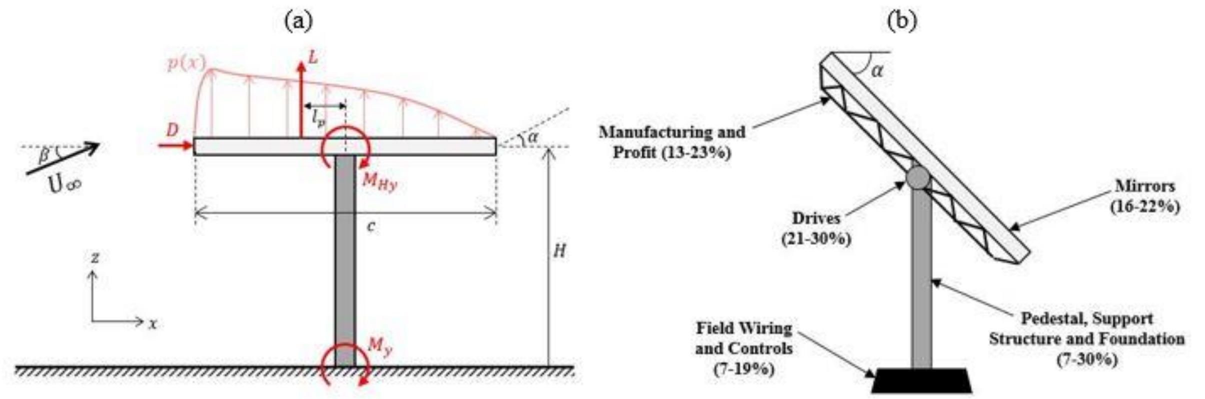

Fig. 1. (a) Main wind loads acting at the centre of pressure l_p due to a non-uniform pressure distribution $p(x)$ on a heliostat in stow position with a chord length c and an elevation axis height H;
(b) Breakdown of heliostat cost by component (reproduced from Kolb et al. (2011)).

Knowledge of the aerodynamic loads on heliostats during high-wind events is critical for their design to maintain structural integrity in stow position, and requires an understanding of the turbulent effects of neutrally-stratified wind over flat, uniform terrain in the atmospheric boundary layer (ABL). Large physical structures such as buildings and heliostats are positioned in the lowest 200 m ($\delta_s \approx 0.2\delta$) of the neutral ABL, known as the atmospheric surface layer (ASL). Full-scale field measurements in the ASL were shown to have similar turbulence properties to the canonical turbulent boundary layer along a flat plate in a wind tunnel (Plate, 1974). For example, the wind velocity profile $\overline{U}(z)$ in the ABL (Fig. 2) can be accurately modelled by the power law and log law to a theoretical maximum gradient or freestream velocity U_∞ at the boundary layer thickness δ (Kaimal and Finnigan, 1994), however Banks (2011) noted that replication of the turbulent power spectra in boundary layer wind tunnels cannot be achieved due to discrepancies in scaling between heliostat models (typically 1:10 to 1:50) and the turbulent eddy length scales (typically 1:100 to 1:300). Heliostats are typically stowed at heights below 10 m in the ASL and hence they are exposed to large velocity gradients and rapid fluctuations of the instantaneous wind velocity relative to the mean, also known as gusts (Kristensen et al., 1991). These flow fluctuations arise from eddies of varying sizes within the ABL that are produced by surface roughness and obstacles in the viscous sublayer near the ground. The sizes of the largest eddies, defined by the longitudinal integral length scale L_u^x, that are the same order of magnitude as the characteristic length of a physical structure have a significant effect on the fluctuating pressures and unsteady forces, which can result in fatigue damage and lead to structural collapse. Small eddies result in pressures on various parts of a structure that become uncorrelated with distance of separation, however large eddies whose sizes are comparable with the structure result in well-correlated pressures over its surface as the eddies engulf the structure, leading to maximum wind loads (Greenway, 1979; Mendis et al., 2007). Maximum wind loads on a stowed heliostat at heights H below 20 m in the ASL will therefore tend to occur from the interaction of the largest eddies with the heliostat facet. Holdø et al. (1982) found that the drag force on a scale model low-rise building of height D increased by 10% in an ABL with a turbulence intensity of 25% (L_u^x/D = 2.8) compared to a uniform approaching flow (L_u^x/D = 1.6). However, Roadman and Mohseni (2009) observed the maximum wind loads on small-scale micro-air-vehicles (MAVs) when the sizes of the eddies were an order of magnitude larger or smaller than their chord length ($c \leq 15$ cm). Hence, consideration of the sizes of the largest eddies in the ABL relative to the characteristic length of a physical structure can lead to significant savings in costs due to the reduced design wind loading.

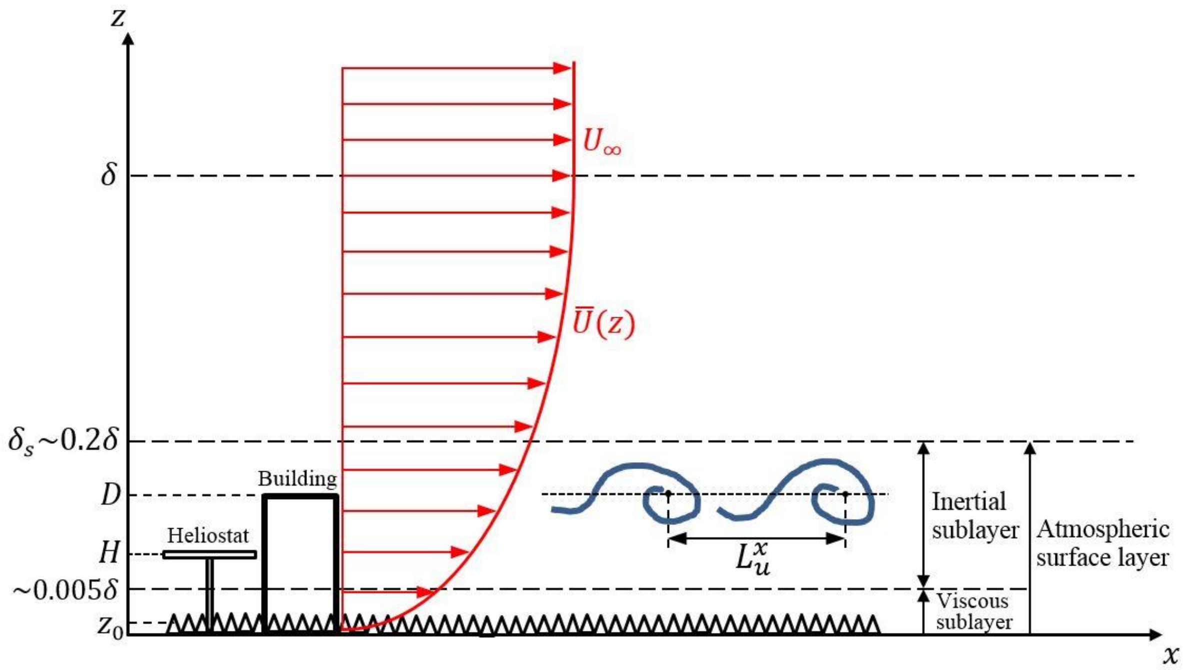

Fig. 2. Structure and turbulence characteristics of the atmospheric boundary layer.

Wind codes and standards for low- to medium-rise buildings adopt a simplified gust factor approach that assumes quasi-steady wind loads based on a maximum gust wind speed, however due to their non-standard shapes, heliostat components have previously been designed from mean and peak wind load coefficients derived from experimental data in systematic wind tunnel studies. Peterka et al. (1989) found that the lowest drag forces on a 1:40 scale heliostat modelled as a thin flat plate occurred at an elevation angle α of 0°, however the peak lift and hinge moment coefficients were approximately 10 times their mean values in stow position. This indicates the significance of gust and amplification effects of survival high-wind conditions for heliostats in stow position. Wind tunnel experiments by Peterka et al. (1989) and Pfahl et al. (2011) showed that peak wind load coefficients increase significantly at turbulence intensities I_u above 10%. Pfahl et al. (2015) found that the peak lift coefficient and peak hinge moment increased by 6.5% and 15%, respectively, when the freestream longitudinal turbulence intensity was increased from 13% to 18% in a range characteristic of the turbulence within heliostat fields in an open country terrain. The temporal variation of turbulence has been widely studied, however the effect of the spatial distribution of turbulence and the length scales of vortices embedded in the turbulence in the ABL has not been investigated in a systematic study. Analysis of the peak wind loads on heliostats in wind tunnel experiments has previously yielded the most realistic results by matching the longitudinal turbulence intensity, however the sizes of the relevant eddies that are the same order of magnitude as the chord length of the heliostat are presumed to be responsible for the peak wind loads (Pfahl et al., 2015). The ratio of integral length scale to building height L_u^x/D was found to have a greater effect than Reynolds number on peak drag coefficient for turbulence intensities between 2% and 25% (Holdø et al., 1982). The effect of increasing the length scale ratio (L_u^x/D) of a 2D short rectangular cylinder of height D to greater than 3 was found by Nakamura (1993) to have a very small effect on the body-scale turbulence ($I_u =$ 10-12%) and galloping vibration. Hence, this paper aims to investigate the effect of the ratio of integral length scale to heliostat chord length L_u^x/c on the peak lift and hinge moment coefficients on a heliostat in stow position.

The dynamic wind-excited response of permanent structures such as heliostats positioned on the ground determines their ability to withstand gusts in the ABL. Tall or slender structures with low natural frequencies are most likely to respond to the dynamic effects of gusts, which can lead to failure from excessive deflections and stresses due to galloping and torsional flutter (Jain et al., 1996; Mendis et al., 2007). Flutter is an oscillatory instability from one or more vibrational modes at a critical wind velocity leading to an exponentially-growing response that often leads to structural failure, whereas buffeting is the random response due to turbulence in the oncoming wind flow that does not generally lead to catastrophic failures but is important for serviceability considerations (Jain et al., 1996). Nakamura (1993) found that galloping and torsional flutter tend to occur on short rectangular cylinders of height D ($Re_\infty = \overline{U}D/\nu$ from 0.14 to 30 × 10^4) at frequencies of the order of 1 Hz when the turbulence length scales are comparable to the size of the body ($L_u^x/D \approx 1$). This has a particular significance for heliostats with natural frequencies between 2 Hz and 5 Hz (Gong et al., 2012) that are stowed in the lowest 10 m of the ASL. The longitudinal integral length scales were calculated by Emes et al. (2017) to be $L_u^x/z \geq 1$ in the lowest 10 m of a low-roughness desert terrain, hence stowed heliostats in open country and low roughness terrains are likely to be exposed to vortices of sizes that are the same order as the heliostat chord length c. The gust factor method assuming quasi-steady wind loads is widely used in design codes (American Society of Civil Engineers, 2013; Cook, 1985; Engineering Sciences Data Unit, 1985; Standards Australia and Standards New Zealand, 2011) to estimate the peak wind loads on large buildings with heights less than 200 m and calculation of an along-wind dynamic response factor with a natural first-mode fundamental frequency between 0.2 Hz and 1 Hz (Holmes et al., 2012). However, this standard approach is not suitable for heliostats as they have chord lengths and heights that are an order of magnitude smaller and typically have natural frequencies that are at least an order of magnitude larger than standard-sized buildings. Discrepancies in peak wind loads estimated using the gust factor method commonly arise from the high impact of the instantaneous angle of attack for longitudinal wind flows with large vertical components of turbulence and the shift of the turbulent energy spectra to higher frequencies in boundary layer wind tunnels (Banks, 2011; Pfahl et al., 2015). This is the case for a heliostat in stow position, as the mean wind load is near zero for longitudinal wind flow but reaches significant values for high vertical turbulence components caused by vortex structures. The eddies corresponding to the peaks of the power spectra that are comparable in size to the heliostat mirror are important for the maximum lift forces and hinge moments on heliostats in stow position, as these eddies cause the maximum pressure differences over the surface of the heliostat mirror. Gong et al. (2013) found that large negative peak wind pressure coefficients occurred at the leading edge of the mirror surface in stow position, suggesting that this region was the most vulnerable to wind-induced mirror damage. The size of the largest eddies relative to the size of the mirror is believed to be the factor that is responsible for these peak wind pressures, however the length scales and dominant frequencies of these eddies were not previously reported. Hence, the present study investigates the distribution of pressure coefficients and peak wind loads on a stowed heliostat and the correlation of loads and eddy frequencies at different points near the leading edge of the heliostat mirror.

The overall aim of this paper is to investigate the dependence of peak wind load coefficients on a heliostat in stow position on three turbulence characteristics in the atmospheric surface layer: freestream Reynolds number, turbulence intensity and the ratio of integral length scale to chord length of the stowed heliostat mirror. To achieve this aim it is required to fully characterise the temporal and spatial distribution of velocity to represent the eddies in the lower ABL, to which stowed heliostats are exposed, during gusty high-wind conditions. Force measurements on different-sized heliostat mirrors at a range of elevation axis heights were used to derive relationships for the peak lift and peak hinge moment coefficients as a function of these turbulent characteristics and the height of the stowed heliostat mirror in the ABL. Pressure distributions over the surface of the stowed heliostat facet were measured for analysis of their correlation with load fluctuations, particularly close to the leading edge of the facet, from the interaction with large vortices so that the turbulence conditions that would most likely lead to critical failures and fatigue could be determined. The results will be used to provide recommendations for improving the accuracy and versatility of the current methods used for calculating the ultimate design wind loads on heliostats in stow position, based on the temporal and spatial turbulence characteristics of gusts in the lower ABL. Further, the derived relationships can be used to optimise the dimensions of the stowed heliostat mirror chord length and elevation axis height, based on known characteristics of the approaching turbulence in a given ABL.

2. Experimental Method

2.1. Experimental setup

Experimental measurements were taken in a closed-return wind tunnel at the University of Adelaide. The test section of the tunnel has a development length of 17 m and a cross-section expanding to 3 m × 3 m to allow for a pressure gradient resulting from growth of the boundary layer. The tunnel can be operated at speeds of up to 20 m/s with a low level of turbulence intensity, ranging between 1% and 3%. The unperturbed boundary layer formed in smooth flow is 0.2 m thick at the location of the turntable, 15 m downstream of the turning vanes. Accurate representation of a part-depth ABL in the wind tunnel is required to replicate similar turbulence properties that heliostats are exposed to in the lower surface layer of the ABL, including a logarithmic mean velocity profile. It is generally accepted that the most effective wind tunnel simulation of the ABL is obtained when a flow passes over a rough surface producing a natural-growth boundary layer (De Bortoli et al., 2002). The most commonly-used passive devices include spires to generate turbulent mixing through separation of flow around their edges, fence barriers to increase the height of the boundary layer and floor roughness to develop the velocity deficit near the ground (Cook, 1978; Counihan, 1973). The present study uses spires and roughness elements shown in Fig. 3(a) to generate a power law mean velocity profile of the form

$$\overline{U}(z) = U_{\infty}\left(\frac{z}{\delta}\right)^{\alpha}, \tag{1}$$

where U_{∞} (m/s) is the freestream velocity, δ is the boundary layer thickness and α is the power law exponent. Dimensions of two different triangular spire designs and the timber roughness blocks are shown in Fig. 3(b). These dimensions were derived following a theoretical design method outlined by Irwin (1981) such that the height h, base width b and depth d of the spire could be determined based on the desired power law profile with exponent α of 0.2 and boundary layer thickness δ of 1.2 m. This gives a ratio of boundary layer thickness to wind tunnel height of 0.33, for which Irwin (1981) showed that the experimental boundary layer velocity profile based on the spire dimensions ratio b/h can be generated to within 3% of a power law velocity profile. Lateral homogeneity of the fully developed boundary layer was found to occur after a minimum streamwise distance of 6 spire heights ($6h$)

downstream of the spires, whereas the effect of the roughness elements on the velocity deficit of the boundary layer becomes smaller with increasing downstream distance. The mounting point of the stowed heliostat is $9h$ downstream of the spires in the current study, hence the development length of the tunnel is expected to be sufficient for lateral flow homogeneity.

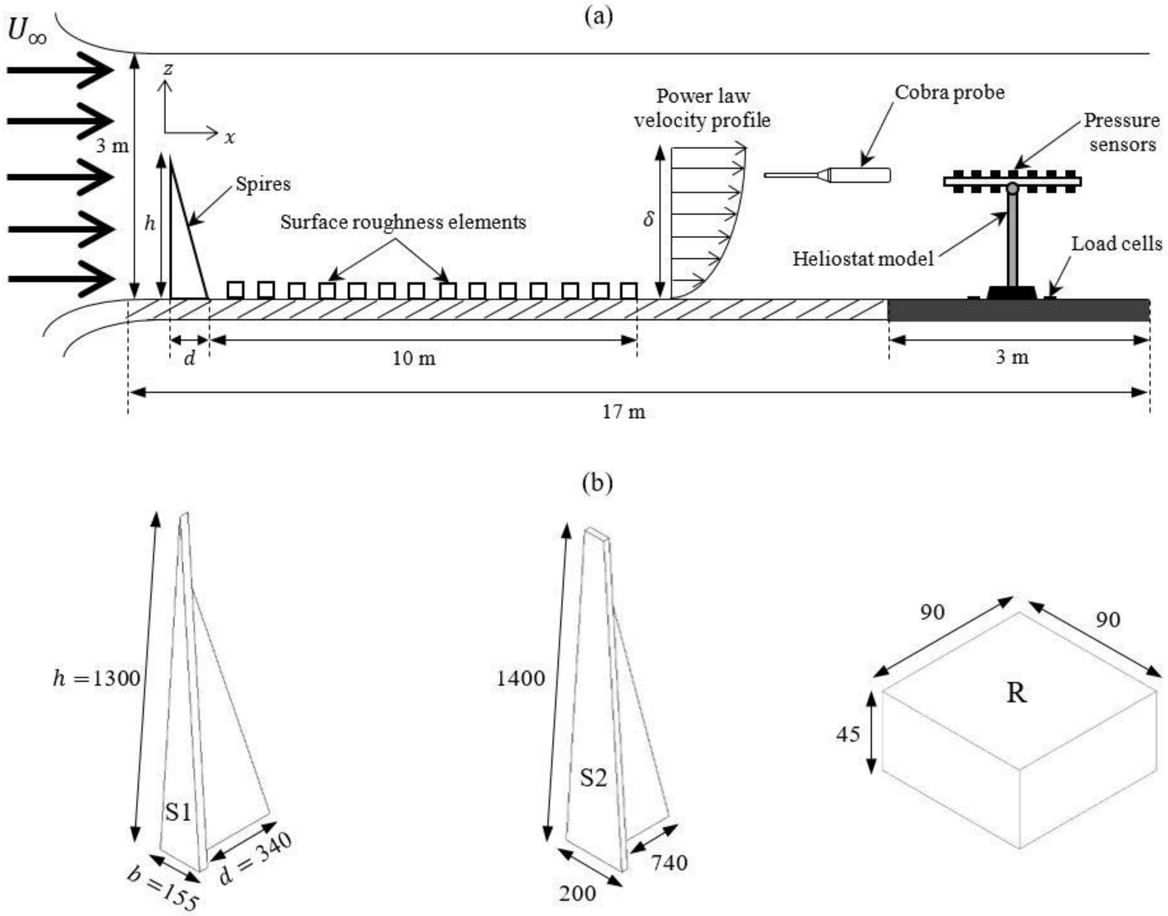

Fig. 3. (a) Schematic diagram with labelled dimensions of the wind engineering test section in the closed-return wind tunnel containing spires and roughness elements and a stowed heliostat; (b) Schematic diagram showing the dimensions (mm) of the two spires and the roughness elements (R) used for generation of the lower ABL.

The experimental setup in the wind tunnel is shown in Fig. 9 for one of the two spire and roughness configurations tested, hereafter referred to as SR1 and SR2, with dimensions shown in Fig. 3(b). The spires were separated by a distance of 650 mm at their centrelines followed by a 10 m fetch of wooden roughness elements. Three components of velocity were measured using a Turbulent Flow Instrumentation (TFI) Cobra probe at a sampling frequency of 1 kHz with an oversampling ratio of 5 to satisfy the Nyquist criterion and prevent aliasing. Data were taken at two freestream velocities U_∞ of 11 m/s and 15.5 m/s, corresponding to freestream Reynolds numbers $Re_\infty = U_\infty \delta / \nu$ of 0.88×10^6 and

1.24×10^6, respectively. The forces and pressures at these velocities fill the measurement span of the devices so that errors remain small.

Fig. 4 presents the mean velocity and turbulence intensity profiles as a function of non-dimensional height z/δ at three spanwise locations in the lower ABL generated by SR1 with a freestream velocity U_∞ of 11 m/s, boundary layer thickness of δ of 1.2 m and Reynolds number Re_∞ of 880,000. Velocity profiles at the tunnel centreline ($y = 0$ m) in Fig. 4(a) show lateral homogeneity within a maximum error of ±5% of the values at the outer boundaries of a 1 m × 1 m grid at the position of the heliostat. The heliostat was stowed at heights relative to the boundary layer thickness z/δ between 0.3 and 0.5, as indicated by the shaded region in Fig. 4. Turbulence intensities at the two outer lateral boundaries in Fig. 4(b) are within 1% and 2% of the centreline values, respectively, which are considered to be sufficient for using centreline profiles for the calculation of turbulence parameters and wind loads. Mean velocity profiles are well approximated by the theoretical power law curve $\overline{U}(z) = 11(z/1.2)^{0.18}$ to represent a low-roughness atmospheric surface layer in an open country terrain, as is commonly modelled for the region surrounding heliostat fields. The power law curve can be shown to correspond to a logarithmic mean velocity profile with roughness height z_0 of 2 mm within a maximum 1% error.

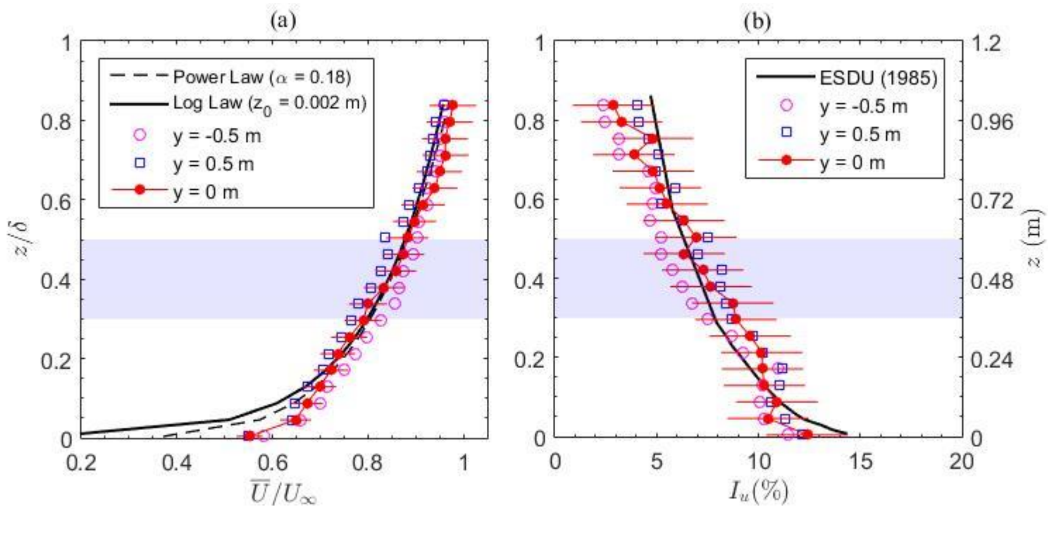

Fig. 4. Flow profiles at three spanwise y locations in the ABL generated using spire and roughness configuration SR1: (a) Mean velocity profiles normalised with respect to the freestream velocity U_∞ and compared with power law ($\alpha = 0.18$) and log law ($z_0 = 0.002$ m) profiles; (b) Turbulence intensity profiles compared with ESDU 85020 (1985) for $U_{10r} = 10$ m/s, $z_0 = 0.002$ m and $\delta = 350$ m. Error bars show maximum errors of ±5% of the centreline velocity profile and ±2% of the centreline I_u profile.

Fig. 5 shows the mean velocity and turbulence intensity profiles (I_u) as a function of non-dimensional height z/δ behind two different configurations of spires and roughness elements, hereafter referred to as SR1 and SR2. It can be seen in Fig. 5(a) that SR1 more closely represents the power law and log law profiles than SR2, within a maximum error of ±5% in the range of heights ($0.3 < z/\delta < 0.5$) at which the heliostat mirror is stowed. Although the relative errors in turbulence intensity profiles using SR1 and SR2 are more significant, the values of I_u in the SR1 profile are within ±2% of the ESDU 85020 profile of I_u within the shaded range of heights ($0.3 < z/\delta < 0.5$) of the stowed heliostat in Fig. 5(b). Turbulence intensities ranged between 6% and 13% at the range of stowed heliostat elevation axis heights in the current study, hence the effect of turbulence intensity on the peak wind loads could be investigated by positioning the heliostat mirror at different heights using SR1 and SR2.

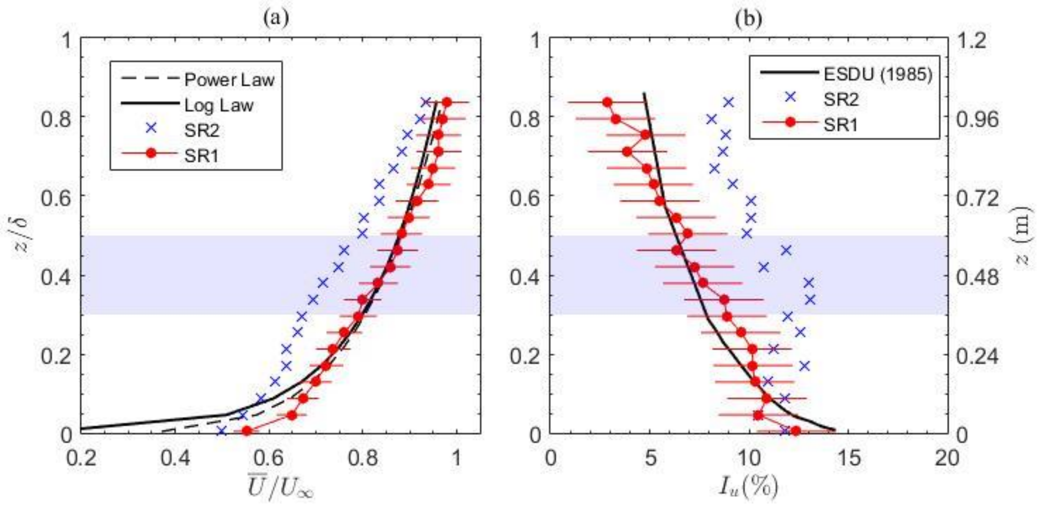

Fig. 5. Centreline flow profiles using two configurations of spires and roughness elements: (a) Mean velocity profiles normalised with respect to the freestream velocity U_∞ and compared with power law ($\alpha = 0.18$) and log law ($z_0 = 0.002$ m) profiles; (b) Turbulence intensity profiles compared with ESDU 85020 (1985) for $U_{10r} = 10$ m/s, $z_0 = 0.002$ m and $\delta = 350$ m. Error bars indicate a maximum error of ±5% of the SR1 velocity profile and ±2% of the SR1 turbulence intensity profile for comparison with the log law profiles.

Fig. 6 compares the Reynolds stress profiles, normalised with respect to the freestream velocity U_∞, as a function of non-dimensional height z/δ of SR1 and SR2 in the current study with the wind tunnel experiment by Farell and Iyengar (1999) in a simulated ABL with $\delta = 1.2$ m and a power law velocity profile with roughness exponent $\alpha = 0.28$. The magnitudes of Reynolds stresses of SR1 in the current study are significantly lower than SR2, however the largest Reynolds stresses occur in the middle region of the ABL at non-dimensional heights z/δ between 0.3 and 0.5 where the heliostat mirror was stowed.

This indicates that the heliostat is exposed to the region of the ABL where the largest turbulent stress production occurs, leading to the generation of the largest eddies. The differences between the Reynolds stress profiles of SR1 and the study by Farell and Iyengar (1999) in this middle region of the ABL are due to the larger velocity gradient $d\overline{U}/dz = 14$ at $z/\delta = 0.5$ in the urban power law ($\alpha = 0.28$) terrain compared to $d\overline{U}/dz = 2.8$ at $z/\delta = 0.5$ in the low-roughness power law ($\alpha = 0.18$) terrain represented by SR1. Further, the packing density, defined as the ratio of roughness element area projected onto a plane perpendicular to the flow direction to the unit ground area surrounding the roughness elements, in the study by Farell and Iyengar (1999) was 7.84% compared to 5% in the current study. In contrast, the magnitudes of Reynolds stresses of SR2 are closer to the study by Farell and Iyengar (1999) because of the larger velocity gradient $d\overline{U}/dz = 5.8$ at $z/\delta = 0.5$ for SR2. Despite the differences in magnitude between the Reynolds stress profiles of SR1 and SR2, the Reynolds stresses are relatively constant at the heights ($0.3 < z/\delta < 0.5$) of the stowed heliostat in the middle region of the simulated ABL. Hence, the effect of the largest eddies can be most independently assessed within this range of heights.

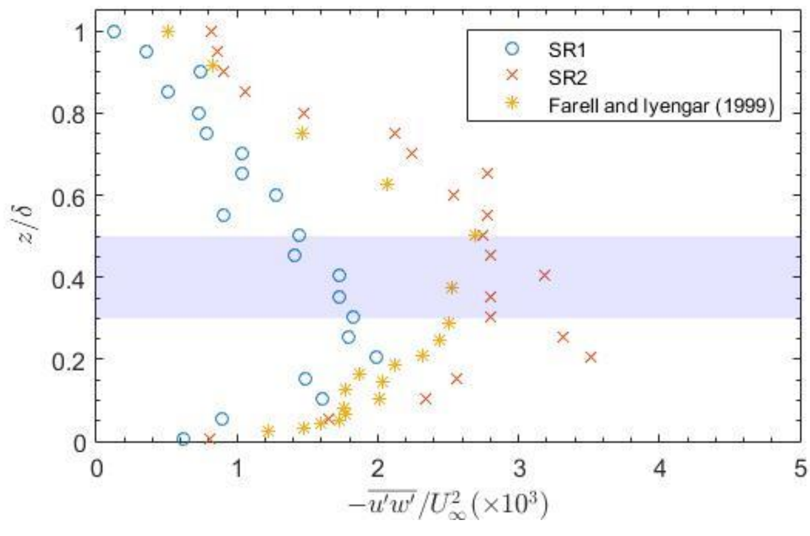

Fig. 6. Reynolds shear stress profiles non-dimensionalised with respect to the freestream velocity and compared with the wind tunnel experiment by Farell and Iyengar (1999) in a simulated ABL with $\delta = 1.2$ m and power law velocity profile ($\alpha = 0.28$). The shaded region indicates the range of heights at which the heliostat mirror was stowed.

Fig. 7 presents the non-dimensional power spectra in the streamwise and vertical directions as a function of non-dimensional frequency $fc/\overline{U}$ based on the chord length ($c = 0.8$ m) of the stowed heliostat and the mean wind speed. It can be seen in Fig. 7(a) and Fig. 7(b) that both the longitudinal power spectra $fS_u/\overline{U}^2$ and the vertical power spectra $fS_w/\overline{U}^2$ for both SR1 and SR2 were similar in magnitude to the Engineering Sciences Data Unit (1985) data for a neutral ABL. The peak energy of eddies at lower frequencies for SR1 is smaller than SR2 because of a lower turbulence intensity of 6%, as the area under the curve of the PSD function is equivalent to the variance ${\sigma_u}^2$ of the streamwise velocity fluctuations. However, the frequency domain of the experimental measurements in the current study is limited due to the differences between heliostat model scales and the wind tunnel flow scales and hence, the low frequency region of the full-scale turbulent power spectra cannot be replicated in boundary layer wind tunnel experiments (Banks, 2011; Pfahl et al., 2015). This is indicated in Fig. 7(a) by a horizontal shift of $fS_u/\overline{U}^2$ for SR1 and SR2 to higher frequencies when the longitudinal turbulence intensity I_u is matched to ESDU 85020. Fig. 7(b) shows that the vertical spectra $fS_w/\overline{U}^2$ are also shifted to higher frequencies, however the vertical turbulence intensities I_w of SR1 and SR2 are 1% larger than the ESDU (1985) data at the same I_u due to the differences in scaling between the longitudinal and vertical components of turbulence in the ABL and the current study. Despite the limitation of wind tunnel experiments at lower frequencies, velocity fluctuations measured at the frequencies corresponding to the peak values of the power spectra were considered sufficient for the calculation of longitudinal integral length scales L_u^x to provide a measure of the largest eddies in the flow.

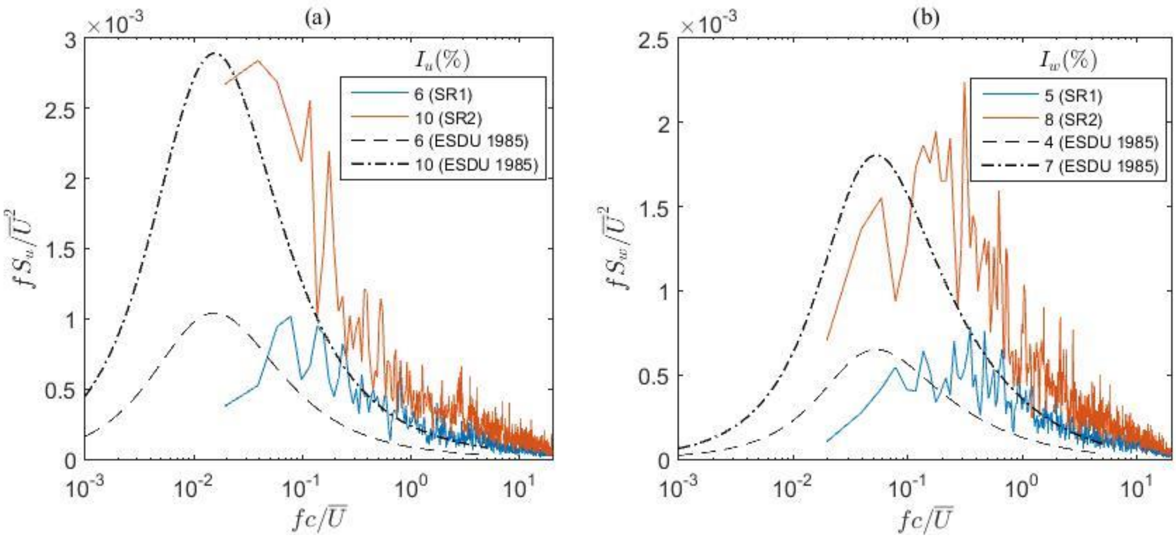

Fig. 7. Non-dimensional power spectra as a function of non-dimensional frequency $fc/\overline{U}$ of the two spire and roughness configurations (SR1 and SR2) compared with Engineering Sciences Data Unit (1985) correlations: (a) Longitudinal power spectra of turbulence $fS_u/\overline{U}^2$; (b) Vertical power spectra of turbulence $fS_w/\overline{U}^2$.

Fig. 8(a) presents the longitudinal integral length scales as a function of height in the ABL with δ of 1.2 m for two combinations of the spires with surface roughness elements (SR1 and SR2). Although there is some scatter, the general trend indicates that the eddies approaching the stowed heliostat at heights between 0.35 m and 0.6 m tend to have length scales between 1.5 m and 3 m. Larger length scales were generated in the middle region of the simulated ABL for SR1 and SR2 compared to S1 and S2 in Fig. 8(a), suggesting that floor roughness can more effectively maintain the larger-scale eddies developed in the near wake of the spires. The average model-scale integral length scales L_{uM}^x for an assumed surface roughness height z_{0M} of 2 mm were converted to a full-scale ABL using the average scale factor $S = 91.3{z_M}^{0.491} / {L_{uM}^x}^{1.403} {z_{0M}}^{0.088}$ from Cook (1978) for comparison with other experimental measurements and a semi-empirical model in Fig. 8(b). Length-scale data in the current study showed good agreement with the wind tunnel simulation of an urban terrain ABL by Counihan (1973) in the lowest 100 m, commonly known as the surface layer, although integral length scales were 37% smaller on average than Counihan (1973) at heights greater than 100 m. This difference is most likely because of the larger gradient or freestream wind speed U_∞ of 31 m/s in the experiments by Counihan (1973) compared to 11 m/s in the current study. The opposite trend was found when comparing the current study with full-scale field measurements by Ivanov and Klinov (1961) over an urban terrain in Moscow and reported in Farell and Iyengar (1999). These discrepancies highlight the difficulties in comparing absolute length scales between full-scale and model-scale experiments.

Integral length scales predicted by the ESDU 85020 model following similarity theory were compared for an assumed logarithmic roughness height z_0 of 1 mm, boundary layer thickness δ of 480 m and mean wind speed $\overline{U}_{10m}$ of 6 m/s at a 10 m height for consistency with the current study. Integral length scales are predicted by ESDU 85020 within a maximum error of ±8% from changing the 10 m height mean wind speed to 6 m/s from the reference 20 m/s wind speed over open country terrain in the ESDU (1985) model. The semi-empirical model under-estimated the length scales by as much as 28% at heights between 100 m and 200 m, as shown Fig. 8(b). Farell and Iyengar (1999) previously observed ESDU 85020 data to be an upper bound to field measurements of L_u^x profiles in open country and urban terrains, however Fig. 8(b) shows that wind tunnel experiments can generate integral length scales as much as double those predicted by the ESDU correlations. The divergence between L_u^x results are most likely because of the scaling issues in wind tunnels and the different techniques used for calculating integral length scales in previous studies. The method commonly used in wind tunnel experiments approximates L_u^x by fitting the von Karman power spectrum to the measured spectra, however Flay and Stevenson (1988) concluded that this method is limited due to difficulties in locating the peaks of the measured spectra. Hence, in the current study L_u^x was estimated using the correlation approach by integrating under the R_u curve to the first-zero crossing (τ_0) because of clearly defined limits of integration, as well as consistent fluctuation of R_u about zero after τ_0, and relatively smaller errors compared to the spectral-fit technique.

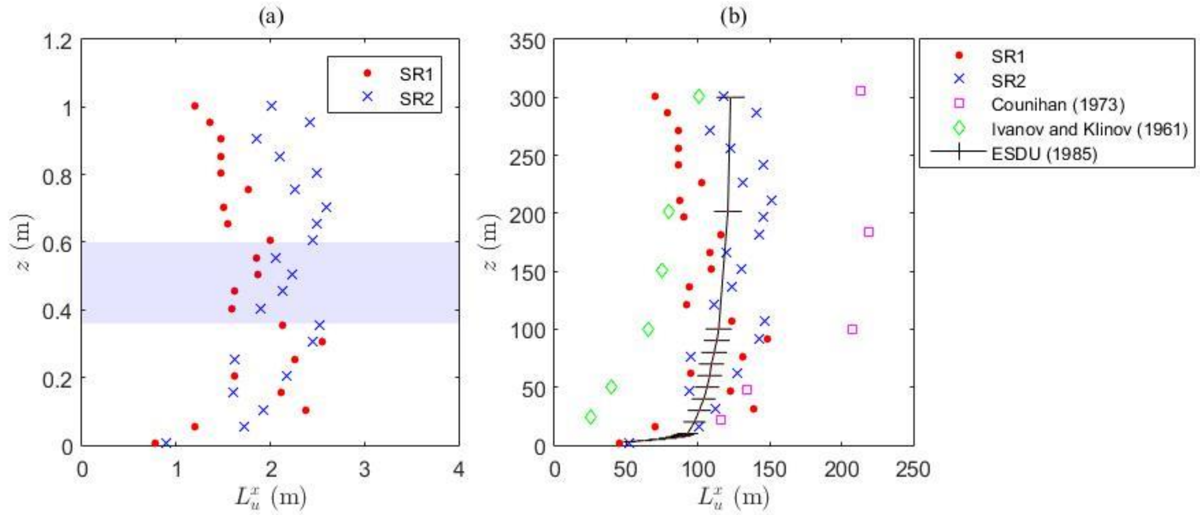

Fig. 8. Longitudinal integral length scale profiles: (a) Integral length scales calculated from the first-zero crossing of the autocorrelation function in the current study ($\delta = 1.2$ m). Shaded region indicates the height at which the heliostat mirror was stowed in the current study;
(b) Comparison of full-scale integral length scales with those measured in full-scale ABLs. Error bars on the ESDU curve indicate a maximum 8% error in the variation of L_u^x with changes in mean wind speed.

Force measurements on the model heliostat were taken using four three-axis Bestech load cells mounted on a rotary turntable, as shown in Fig. 9. Each load cell has a capacity of 500 N with a sampling frequency of 1 kHz in all three axes and an accuracy of ±0.5% of full scale. The heliostat mirror was simply modelled as a thin flat plate in the absence of a support structure, since Gong et al. (2013) showed that the shielding effect of the support structure had a less significant effect on the fluctuating wind pressures on a stowed heliostat exposed to parallel flow ($\beta = 0°$) than standard operating positions and for wind angles β between 90° and 180°. A series of six square aluminium plates with 3 mm thickness and chord length c ranging from 300 mm to 800 mm in 100 mm increments were manufactured and mounted on a common pylon with a telescopic design that allows the elevation axis height H to vary between 0.35 m and 0.6 m (H/δ = 0.3 – 0.5) and H/c to vary between 0.5 and 1.3.

Pressure measurements were taken on the upper and lower surfaces of a thick hollow aluminium facet containing 24 Honeywell high-frequency differential pressure sensors, as shown in Fig. 10(a). Each sensor has a pressure range of ± 1 psi (6.9 kPa) with an accuracy of ±0.2% of full scale. The layout of the pressure taps on the surface of the heliostat is shown in Fig. 10(b). Differential pressures at each of the 24 tap locations were acquired simultaneously at a sampling frequency of 1 kHz for consistency with velocity and force data. To ensure simultaneous measurement and synchronisation of pressure signals at all of the locations on the stowed heliostat, individual channels were connected into two slots of a data acquisition chassis and a trigger was implemented using LabVIEW software to start sampling all of the signals at the same time.

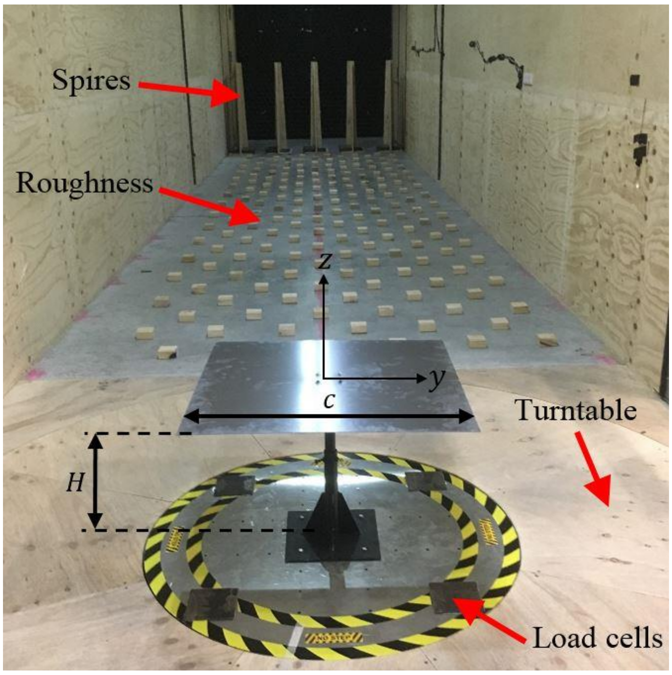

Fig. 9. Experimental setup in the wind tunnel showing spire and roughness configuration SR2 for generation of the lower ABL upstream of a 1:40 scale model heliostat in stow position of 0.8 m chord length (c) and 0.5 m elevation axis height (H).

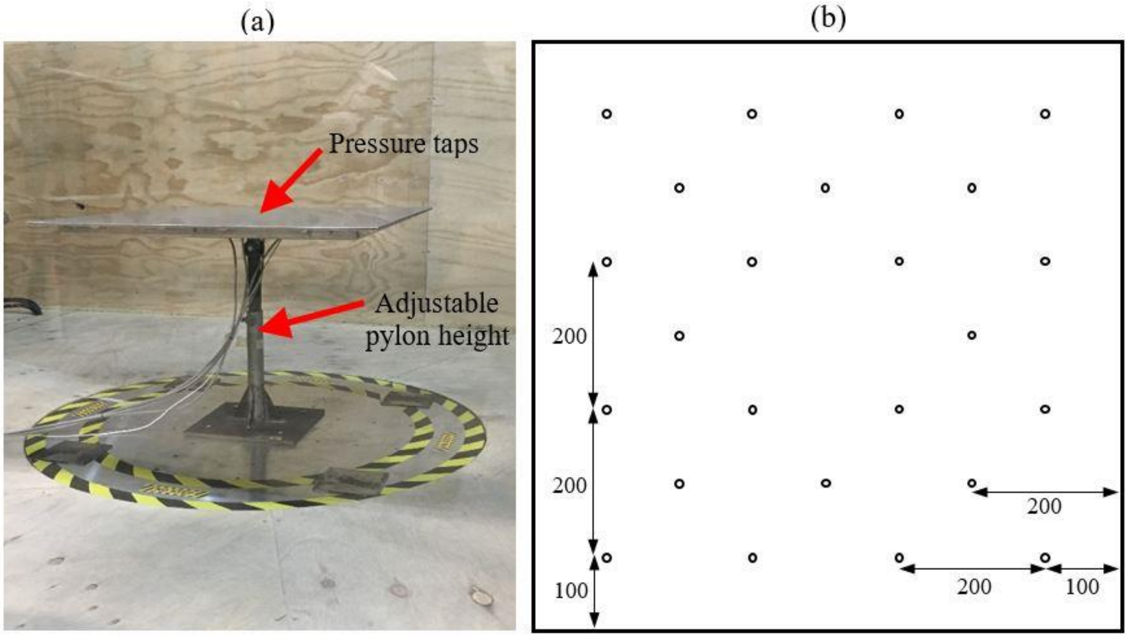

Fig. 10. (a) Experimental setup for surface pressure measurements showing the heliostat facet (c = 0.8 m) containing pressure sensors; (b) Layout of 24 pressure taps on the heliostat facet surface.

2.2. Calculation of integral length scales

The integral length scales represent the sizes of the relevant eddies in the longitudinal direction that correspond to the largest magnitudes of the turbulent power spectra (Milbank et al., 2005; Watkins, 2012). The lower end of the power spectra represents the largest eddies, however these low-frequency eddies may have smaller energies than those at the peaks of the power spectra. Although the lowest frequencies of the turbulent power spectra in the ABL cannot be replicated in the wind tunnel (Milbank et al., 2005; Pfahl et al., 2015), the eddy scales of highest energy are assumed to have the largest impact on the integral length scale. Several different techniques have been used for calculating integral length scales, such as the commonly used spectral-fit method, however there are large uncertainties associated with locating the peaks of the measured spectra at low frequencies (Farell and Iyengar, 1999; Flay and Stevenson, 1988). Hence, the autocorrelation of velocity measurements was used to estimate the longitudinal integral length scales, L_u^x, in the current study because of clearly-defined limits of integration and consistent fluctuation of R_u about zero after τ_0, and relatively smaller errors compared to the spectral-fit technique. Point velocity measurements in the current study, obtained as a function of time, are transformed to spatially-distributed data by Taylor's hypothesis. This assumes that eddies are embedded in a frozen turbulence field convected downstream at the mean wind speed $\overline{U}$ (m/s) in the streamwise x direction, and hence do not evolve with time (Kaimal and Finnigan, 1994; Milbank et al., 2005). The longitudinal integral length scale L_u^x (m) at a given height H is defined in Fig. 11 as the average streamwise spacing between the largest two-dimensional spanwise eddies with a Rankine velocity distribution, which is calculated as (Milbank et al., 2005; Swamy et al., 1979)

$$L_u^x = T_u^x \overline{U}, \tag{2}$$

where T_u^x (s) is the integral time scale representing the time taken for the largest eddies to traverse a single point in the ABL. The integral time scale is calculated using Equation (3) by the integral of the autocorrelation function in Equation (4) up to its first-zero crossing τ_0, assuming that $R(\tau)$ fluctuates close to zero after this point (Swamy et al., 1979). Here $u' = u - \overline{U}$ defines the fluctuating component of streamwise velocity and ${\sigma_u}^2$ is the variance of the streamwise velocity fluctuations.

$$T_u^x = \int_0^\infty R(\tau)\, d\tau \approx \int_0^{\tau_0} R(\tau)\, d\tau, \tag{3}$$

$$R(\tau) = \frac{\overline{u'(t)u'(t+\tau)}}{{\sigma_u}^2} \tag{4}$$

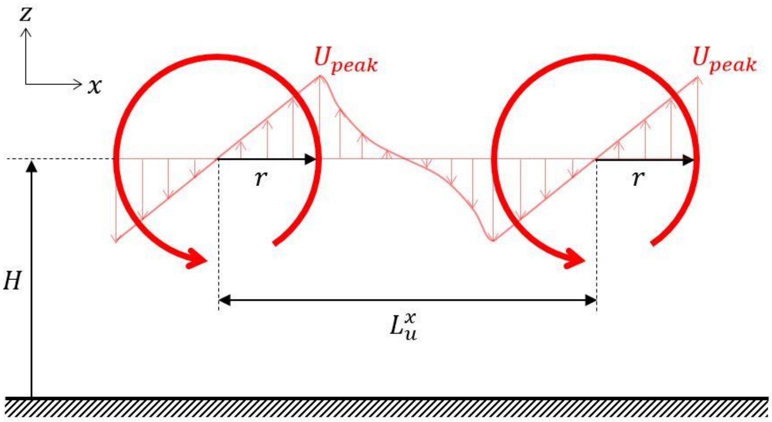

Fig. 11. Schematic diagram of two vortices with a Rankine velocity distribution and the definition of the longitudinal integral length scale L_u^x at elevation axis height H in the flow direction x.

2.3. *Calculation of wind load coefficients*

Mean and peak lift coefficients on the stowed heliostat are calculated from force data using the following equation:

$$c_L = \frac{L}{1/2 \rho \overline{U}^2 A}. \tag{5}$$

Here $L = L_{heliostat} - L_{pylon}$ (N) is the lift force on the flat plate calculated as the difference between the measured lift force on the stowed heliostat and the measured lift force on the pylon without the plate, ρ (kg/m^3) is density, $\overline{U}$ (m/s) is the mean wind speed at elevation axis height H and $A = c \times c$ (m^2) is the area of the flat plate projected onto the x-y plane. The peak lift forces were determined using the three-sigma approach, $L_{peak} = L_{mean} + 3\sigma_L$, for a sampling duration of 1 minute at model scale (10 minutes equivalent full scale) at a sampling frequency of 1 kHz. The pressure coefficients at each pressure tap location i on the stowed heliostat surface are calculated from the measured differential pressures as:

$$C_{P_i} = \frac{P_i^f - P_i^b}{1/2\rho\overline{U}^2}, \tag{6}$$

where P_i^f (Pa) is the pressure on the upper surface of the stowed heliostat mirror and P_i^b (Pa) is the pressure on the lower surface of the stowed heliostat mirror.

Mean and peak hinge moments on the stowed heliostat are calculated as the product of the measured lift force on the stowed heliostat and the distance of the centre of pressure from the centre of the plate defined in Fig. 1. The hinge moment coefficients are defined following Peterka and Derickson (1992):

$$c_{M_{Hy}} = \frac{M_{Hy}}{1/2\rho\overline{U}^2 Ac}. \tag{7}$$

Here $M_{Hy} = L \times l_p$ (N·m) is the calculated hinge moment on the flat plate aligned parallel to the ground, L (N) is the lift force on the plate, c (m) is the plate chord length and l_p (m) is the distance to the centre of pressure in the streamwise direction of the mean flow in Fig. 1, defined as:

$$l_p = \frac{\int_0^c xp(x)\,dx}{\int_0^c p(x)\,dx}. \tag{8}$$

Here $p(x)$ is the non-uniform pressure distribution on the plate ($c = 0.8$ m) in the streamwise direction x (m). The time-averaged location of the centre of pressure was calculated to be $l_p = 0.12c$ for SR1 and $l_p = 0.15c$ for SR2 using the pressure distributions on the instrumented heliostat (Fig. 10).

3. Results and Discussion

3.1. Analysis of peak wind load coefficients

Fig. 12 shows the variation of mean and peak wind load coefficients for the two spire and roughness configurations on the heliostat mirror as a function of chord length c when stowed at a constant height (H/δ) in the ABL. Both mean and peak lift coefficients in Fig. 12(a) increased logarithmically with increasing chord length c from 0.3 m to 0.8 m. The ratio of peak-to-mean lift coefficients varied between 12 and 20 over the range of c tested. A similar exponential trend was observed in Fig. 12(b) for the hinge moment coefficients, as the peak-to-mean ratios were between 15 and 20 for comparison with the ratio of 10 reported in wind tunnel experiments by Peterka et al. (1989) and Peterka and Derickson (1992). Since the peak wind loads are decisive for the design of heliostats in stow position, the following equations have been developed for the peak lift and peak hinge moment coefficients as a function of the velocity gradient ($d\overline{U}/dz$), turbulence intensity I_u (%) and heliostat chord length c (m):

$$c_L = 0.74([d\overline{U}/dz]/10)^{2.1}\, c^{-146 I_u^{-2}}, \tag{9}$$

$$c_{M_{Hy}} = 0.16([d\overline{U}/dz]/10)^{2.39}\, c^{-146 I_u^{-2}}. \tag{10}$$

By assuming that the peak wind loads are caused by the break-up of vortices at the leading edge of the heliostat mirror and the resulting pronounced pressure near the leading edge, it can be shown that an increase of the peak lift force results from an increase in the width b of the mirror panel while it is rather independent of the height H of the mirror. As the chord length c is proportional to H, L is also proportional to H or c, respectively. Hence with constant k and $p_{dyn} = 1/2\, \rho \overline{U}^2$:

$$L \propto b \;\Rightarrow\; L = kb = c_L p_{dyn} bc$$

$$\Rightarrow c_L = k/p_{dyn}\, c$$

$$\Rightarrow c_L \propto 1/c \tag{11}$$

The hinge moment also depends on the distance $l_p(c)$ of the high pressure region near the leading edge to the centre of the mirror panel and it follows similar:

$$M_{Hy} \propto bc \;\Rightarrow\; M_{Hy} = kbl_p(c) = c_{M_{Hy}} p_{dyn} bc^2$$

$$\Rightarrow c_{M_{Hy}} = k/p_{dyn}\, c$$

$$\Rightarrow c_{M_{Hy}} \propto 1/c \qquad (12)$$

These inverse relationships derived in Equations (11) and (12) are approximately in accordance with the peak wind load coefficients in Fig. 12(a) and Fig. 12(b), respectively.

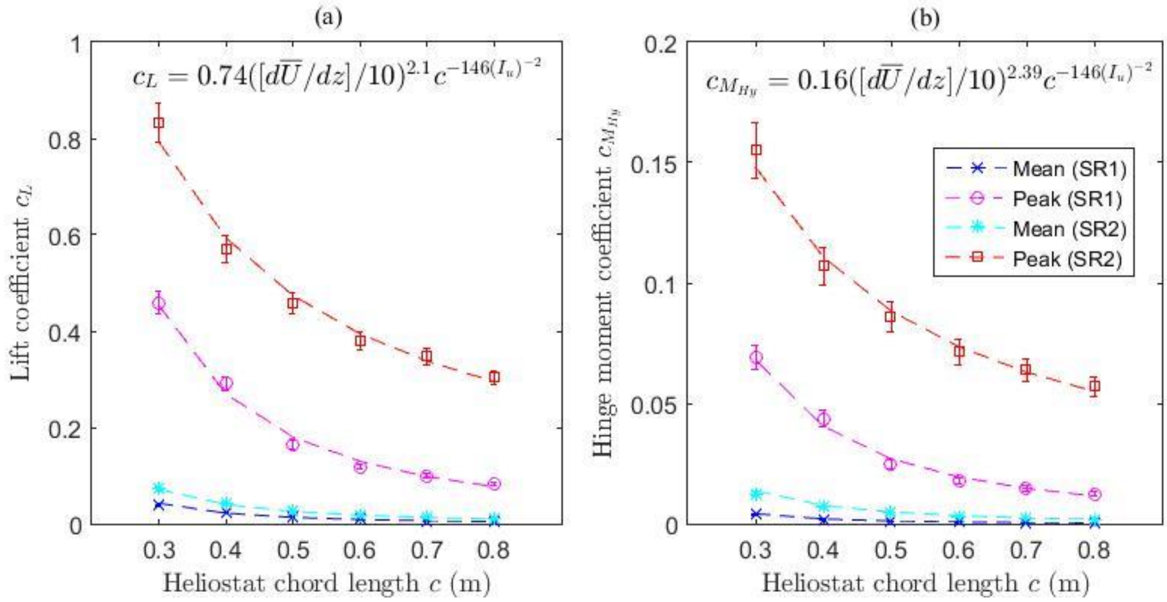

Fig. 12. Mean and peak wind load coefficients on a stowed heliostat as a function of square mirror chord length c for two spire and roughness configurations SR1 and SR2 at $U_\infty \approx 11$ m/s and $H/\delta \approx 0.3$ ($\delta = 1.2$ m): (a) Lift coefficient c_L; (b) Hinge moment coefficient $c_{M_{Hy}}$.

Fig. 13 presents the peak lift coefficient c_L and peak hinge moment coefficient $c_{M_{Hy}}$ as a function of the ratio of elevation axis height to chord length H/c at three different heights, non-dimensionalised with the ABL thickness H/δ, when exposed to SR1 (Fig. 13(a) and Fig. 13(c)) and SR2 (Fig. 13(b) and Fig. 13(d)). The effect of increasing the height at which the heliostat mirror is stowed in the ABL, H/δ, from 0.3 to 0.5 results in a vertical shift of peak c_L and peak $c_{M_{Hy}}$ to larger magnitudes at constant H/c. The effect of this upward shift increases with increasing H/c, hence the effect of H/δ becomes small at $H/c \leq 0.5$. Both peak c_L and peak $c_{M_{Hy}}$ increase exponentially with increasing H/c at a constant H/δ. Conventional heliostats are commonly designed for the ratio H/c of 0.5 (Téllez et al., 2014), however $H/c \approx 0.7$ for a heliostat with a horizontal primary axis. Additionally, $H/c > 0.5$ is required for those heliostats that are moved to the normal position for cleaning and washing of the mirror. Since heliostats would never be required to reach the normal position in the operation of a heliostat field, Fig.

13 shows that the minimum stow design wind loads and thus the lowest capital cost of manufacturing the components of a heliostat can be achieved by designing for H/c of 0.5 for the range of chord lengths tested in the current study. For example, reductions of approximately 50% in c_L and 40% in $c_{M_{Hy}}$ are possible by lowering H/c from 0.7 to 0.5 for a heliostat without a horizontal primary axis. Hence, the overall mass and strength of the heliostat can be reduced as the length of the pylon required is shorter. Designing for the smaller H/c of 0.5 can therefore lead to savings in the cost of manufacturing and installation of the heliostat.

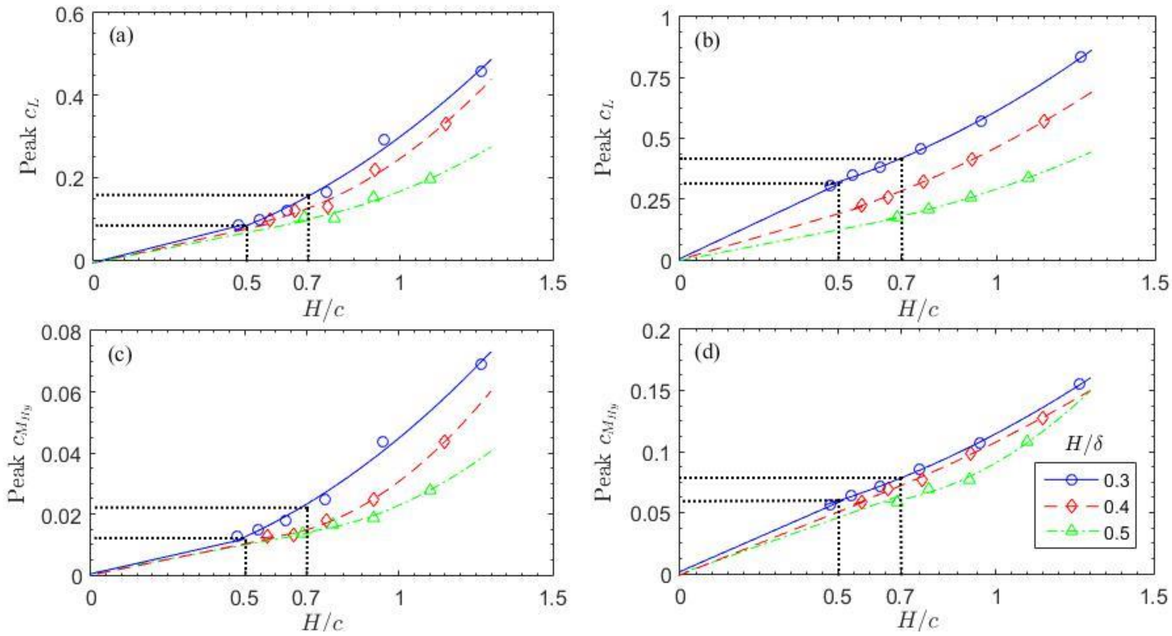

Fig. 13. Effect of the ratio of the elevation axis height to chord length (H/c) on the peak wind load coefficients on a heliostat mirror stowed at three different heights (H/δ) in the simulated ABL at a freestream velocity U_∞ of 11 m/s and Reynolds number Re_∞ of 8.8×10^5:
(a) Peak lift coefficient c_L for SR1; (b) Peak lift coefficient c_L for SR2;
(c) Peak hinge moment coefficient $c_{M_{Hy}}$ for SR1; (d) Peak hinge moment coefficient $c_{M_{Hy}}$ for SR2.

Fig. 14 presents the peak wind loads on the stowed heliostat as a function of the longitudinal turbulence intensity using data for SR1 and SR2 at different heights in the simulated ABL for the six chord lengths tested. Peak lift coefficients in Fig. 14(a) increased linearly at $I_u \geq 10\%$ for the range of chord lengths c between 0.3 m and 0.8 m. The effect of I_u on peak lift coefficient becomes larger with decreasing c because of larger length scale ratios L_u^x/c. In comparison, Fig. 14(b) shows that the peak hinge moment coefficients also increased significantly at $I_u \geq 10\%$. The pronounced linear increase of the peak wind load coefficients on stowed heliostats at turbulence intensities larger than 10% in the current study is in agreement with a similar finding by Peterka et al. (1989) for the peak drag and lift coefficients on heliostats in operating positions.

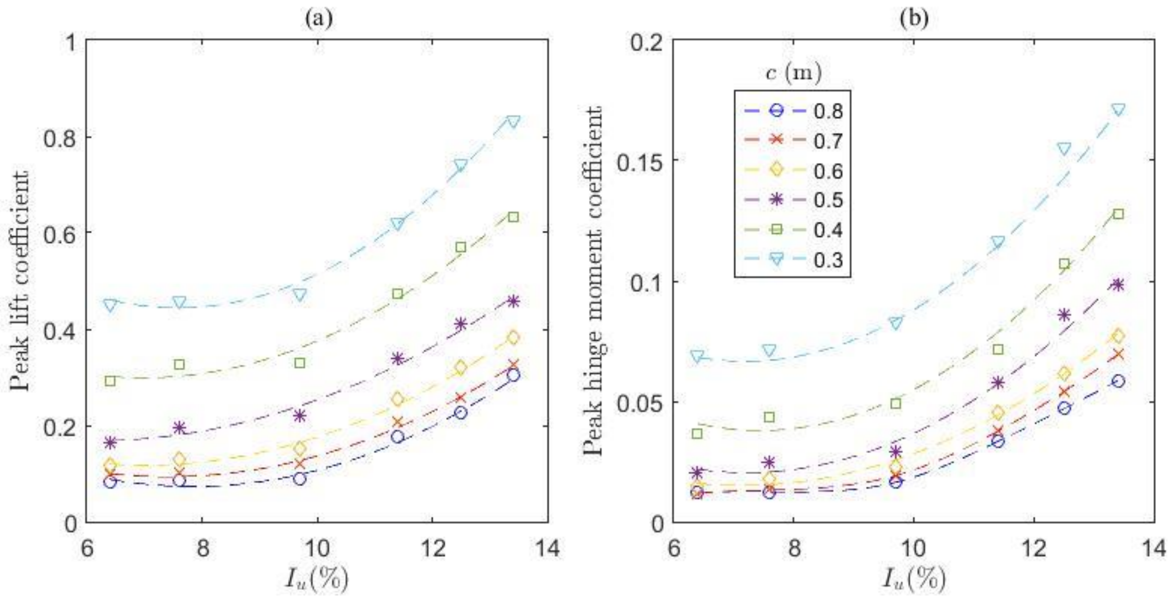

Fig. 14. Effect of turbulence intensity I_u on: (a) peak lift coefficient; (b) peak hinge moment coefficient on a stowed heliostat as a function of heliostat mirror chord length c.

The peak lift and hinge moment coefficients on the smallest stowed heliostat ($c = 0.3$ m) exposed to the maximum I_u of 13.4% in the current study were 8% and 15% smaller, respectively, than those measured by Peterka et al. (1989) at a larger turbulence intensity I_u of 18%. In comparison, the peak lift and hinge moment coefficients on the stowed heliostat with $c = 0.5$ m were 13% and 23% smaller, respectively than those measured by Pfahl et al. (2015) at I_u of 13% similar to SR2 in the current study, as shown in Table 1. The main differences between this study and those by Pfahl et al. (2015) and Peterka et al. (1989) were the elevation axis height to boundary layer thickness ratio H/δ and the integral length scales representing the size of the largest eddies at a given height in the simulated ABL. The lowest value of H/δ of 0.3 in the current study is approximately double that of these previous experimental studies, however their integral length scales were not reported and can vary depending on the fetch length, spire geometry and incoming flow quality. Hence, these differences indicate that BLWT data can lead to uncertainties in the load measurements as the length scales that can be generated are limited by the size of the wind tunnel and the largest length scales that exist in the ABL cannot be simulated.

Table 1. Peak wind load coefficients on stowed heliostats (H/c = 0.5) in wind tunnel experiments

Turbulence intensity I_u (%)	Height in boundary layer H/δ	Peak lift coefficient c_L	Peak hinge moment coefficient $c_{M_{Hy}}$	Source
12.5	0.3	0.4	0.1	Current study (SR2)
18	0.15	0.9	0.2	Peterka et al. (1989)
13	0.15	0.46	0.13	Pfahl et al. (2015)

Fig. 15 presents the effect of the ratio of longitudinal integral length scale to heliostat chord length L_u^x/c on the mean and peak lift and hinge moment coefficients using data for SR1 and SR2 at different heights in the simulated ABL for the six chord lengths tested. It can be seen in Fig. 15(a) that the peak lift coefficient increases linearly from 0.1 to 0.8 as L_u^x/c increases from 2.5 to 10. In comparison, the peak hinge moment coefficient in Fig. 15(b) increases linearly from 0.02 to 0.12 as L_u^x/c increases to 10. These linear relationships of the peak lift and hinge moment coefficients with L_u^x/c can be approximated by the following equations:

$$c_L = 0.1(L_u^x/c) - 0.113 \tag{13}$$

$$c_{M_{Hy}} = 0.022(L_u^x/c) - 0.032 \tag{14}$$

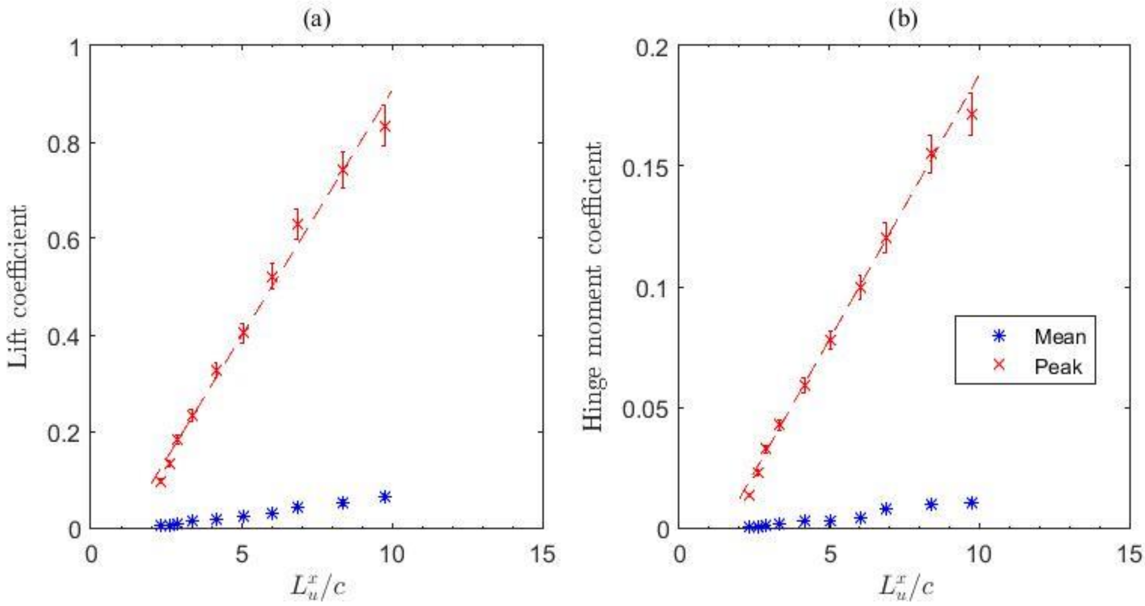

Fig. 15. Effect of length scale ratio L_u^x/c on the mean and peak wind load coefficients on a stowed heliostat with chord length c: (a) Lift coefficient; (b) Hinge moment coefficient.

Fig. 16 presents the peak lift and hinge moment coefficients, averaged for SR1 and SR2, as a function of turbulence intensity I_u and freestream Reynolds number Re_∞ for a stowed heliostat of three different chord lengths c. Fig. 16(a) shows that increasing freestream Reynolds number by 40% leads to average increases of 13%, 15% and 21% in c_L for c of 0.3 m, 0.5 m and 0.8 m, respectively, at a constant turbulence intensity I_u ranging from 6.5% to 13%. In comparison, the average increases in $c_{M_{Hy}}$ are 14%, 16% and 25%, respectively for the same values of c, as shown in Fig. 16(b). These relative changes in peak wind load coefficients are considerably less than the dependence on L_u^x/c in Fig. 15, providing confidence that the hypothesis proposed by Holdø et al. (1982) regarding the peak drag coefficient at turbulence intensities between 2% and 25%, can be confirmed for the peak lift coefficient with a larger range of freestream velocities or boundary layer thicknesses. The limited tunnel size would not allow major changes to the thickness of the simulated ABL, lower freestream velocities could not be tested due to increasing uncertainties in the force measurements, and higher freestream velocities could not be used due to instability of the spires and roughness elements.

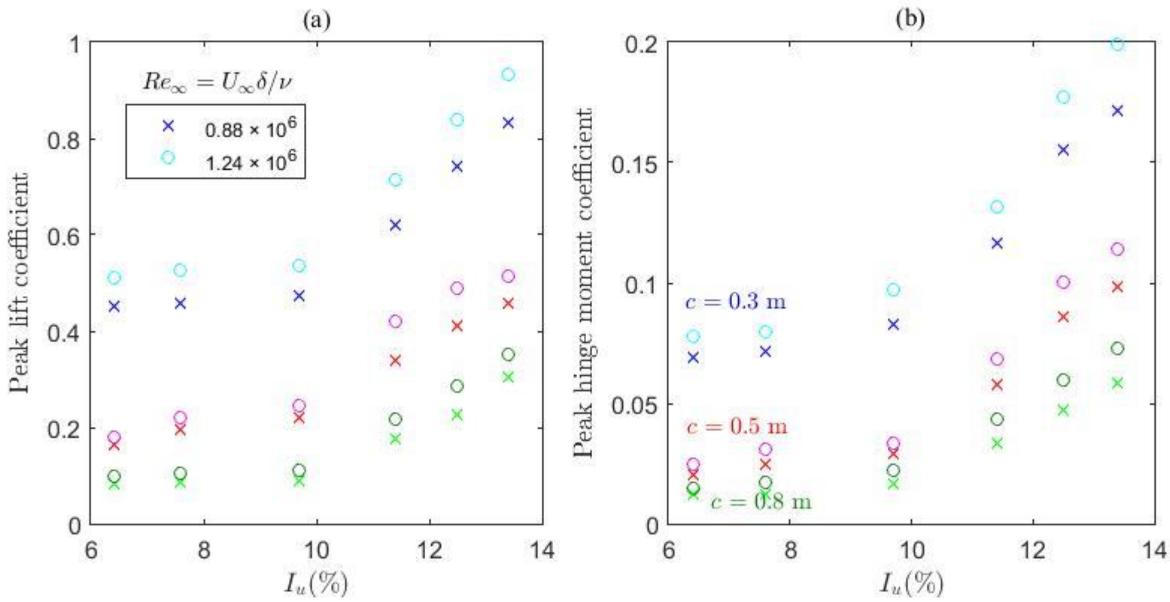

Fig. 16. Effect of freestream Reynolds number $Re_\infty = U_\infty \delta/\nu$ as a function of turbulence intensity I_u on: (a) Peak lift coefficient; (b) Peak hinge moment coefficient.

3.2. *Surface pressure distributions on stowed heliostat*

Fig. 17 shows the contours of mean, RMS and peak pressure coefficients C_P calculated using Equation (6) at each of the 24 pressure taps and linearly interpolated between the points on the stowed heliostat for SR2. Large magnitudes of C_P were concentrated in the frontal 10% of the plate behind the leading edge due to the break-up of large eddies at the leading edge. This can result in large lift forces close to the leading edge of the mirror, thus resulting in the maximum hinge moments that can potentially lead to failure with insufficient structural integrity and strength of the mirror and supporting structure. The high intensity area of peak C_P in Fig. 17(c) is concentrated on the central 0.5 m of the leading edge that results in a peak lift coefficient of 0.26. This confirms the finding by Gong et al. (2013) that the leading edge of a stowed heliostat is most vulnerable to wind-induced mirror damage from the interaction with large vortices. This case is also important for serviceability considerations in the design of heliostats for multiple cycles of up-lift loading in the stow position.

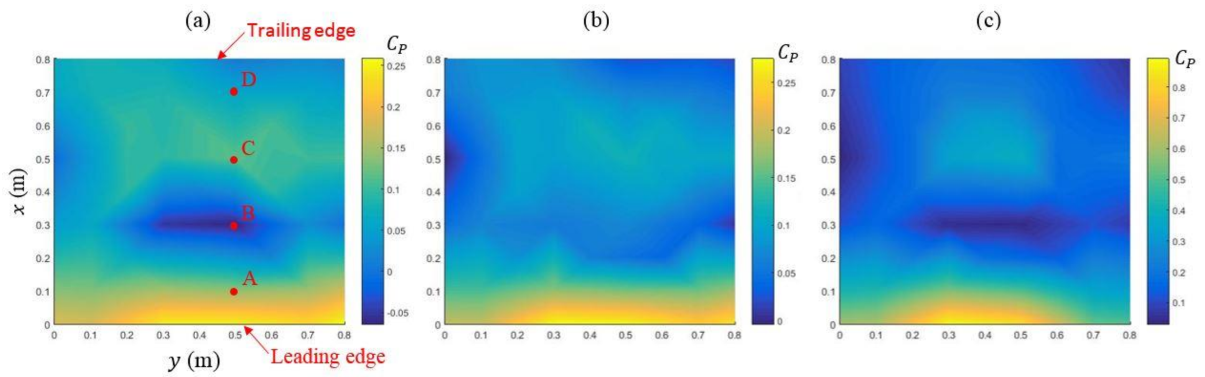

Fig. 17. Surface pressure coefficient C_P contours on the stowed heliostat for SR2: (a) Mean; (b) RMS; (c) Peak.

Fig. 18(a) presents the time histories of measured differential pressure fluctuations about a zero-mean value at four points along the heliostat mirror surface from the leading edge to the trailing edge, as shown in Fig. 17(a). Table 2 shows that the largest amplitudes of pressure fluctuations in Fig. 18(a) occur at points A and D near the leading and trailing edges, respectively. The peak power spectrum of the pressure signals at point A is over 6 times the magnitude of the other three points, as shown in Fig. 18(b). The peak power spectra values occur at frequencies of 2.4 Hz near the leading edge are shifted to higher frequencies with downstream distance along the mirror surface to 21 Hz near the trailing edge. Fig. 18(c) presents the cross-correlations between two points in the along-wind direction (x) as a function of time lag τ between the instantaneous pressure signals. The pressure fluctuations are most highly correlated between points A and B with a peak normalised cross-correlation coefficient of 0.88 and the shortest phase delay of 0.018 s in Table 3. Although pressure fluctuations become less correlated further along the plate as the phase delay increases, the peak coefficient only decreases by 15% from A-B to A-D. This suggests the presence of a vortex-heliostat interaction near the leading edge of the mirror surface, as illustrated by the pressure coefficient contours in Fig. 17. Since the fluctuating pressures corresponded to low-frequency peaks on the power spectra and remain highly correlated across the along-wind length of the mirror, large-scale spanwise vortices can cause progressive failure initiating at the leading edge.

Table 2. Characteristics of stowed heliostat surface pressure fluctuations

Measurement point and coordinates $(\boldsymbol{x},\boldsymbol{y})$	Maximum amplitude $\boldsymbol{P'}$ (Pa)	Frequency of peak power spectra $\boldsymbol{f}$ (Hz)
A (0.1 m, 0.5 m)	39.1	2.4
B (0.3 m, 0.5 m)	11.1	2.5
C (0.5 m, 0.5 m)	16.6	6.8
D (0.7 m, 0.5 m)	18.4	21

Table 3. Cross-correlation statistics of stowed heliostat surface pressure fluctuations

Two points for cross-correlation	Phase delay $\boldsymbol{\tau}$ (s)	Peak normalised cross-correlation coefficient $\boldsymbol{R_{p1p2}}$
A-B	0.018	0.88
A-C	0.034	0.82
A-D	0.071	0.75

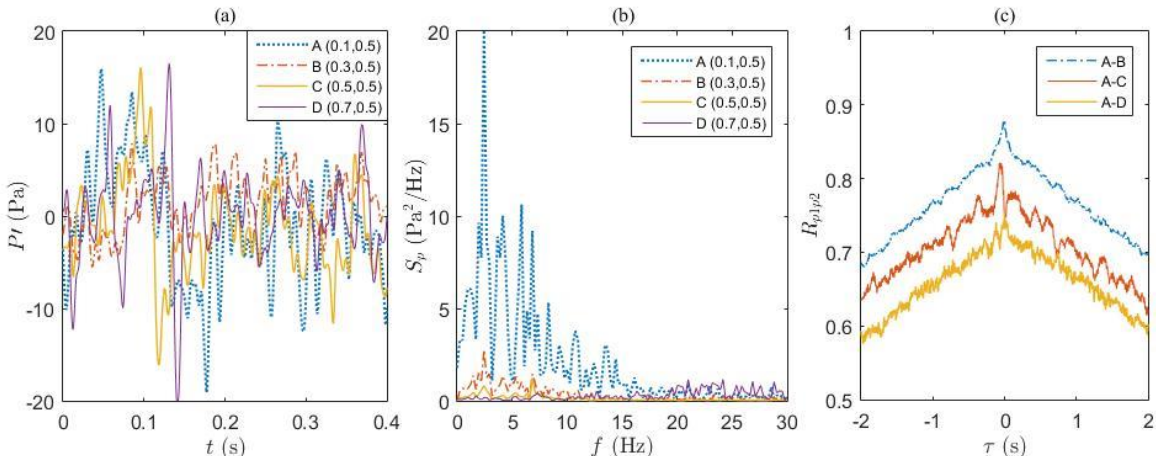

Fig. 18. (a) Time history of pressure fluctuations P' (Pa) between the upper and lower surfaces at four points along the stowed heliostat mirror surface; (b) Power spectra of pressure fluctuations S_p (Pa^2/Hz) at four points along the stowed heliostat mirror surface; (c) Normalised cross-correlation coefficients R_{p1p2} of pressure fluctuations between two points from the leading edge to the trailing edge of the mirror surface.

4. Discussion and Conclusions

Calculations of peak wind load coefficients have established that the sizes of the vortices corresponding to the largest energies within the flow were at least double the heliostat mirror chord length in the current study. This study varied the length scale ratio L_u^x/c using smaller-sized heliostat mirrors modelled as thin flat plates. The break-up of the large vortices at the leading edge of the mirror results in a non-uniform pressure distribution $p(x)$ along the mirror surface. As L_u^x/c increased from 2.5 to 5, the peak wind loads increased linearly as the large suctions caused by the large-eddy break-up at the leading edge increase in magnitude. The most significant increase, resulting in a doubling of the peak lift and hinge moment coefficients, occurred for L_u^x/c between 5 and 10. Contours of wind pressure coefficients in Fig. 17 confirmed that large pressures at the leading edge need to be considered for critical failures of the heliostat in the stow position. The lower frequencies of the fluctuating pressure signals are of the order of 2 Hz close to the leading edge, which is close to the natural frequencies of 2-5 Hz measured on stowed heliostats by Gong et al. (2012). Hence, the leading edge is more likely to be exposed to resonance effects that can lead to excessive deflections and stresses that commonly result in structural failure.

Turbulence intensity and the sizes of the largest vortices were found to have a more pronounced effect on peak wind load coefficients than freestream parameters such as mean velocity and Reynolds number. Both peak lift and hinge moment coefficients were calculated to be at least ten times the size of their mean coefficients, confirming those found by Peterka et al. (1989) for a stowed heliostat. Peak wind load coefficients increased linearly and by approximately double in magnitude with an increase of I_u from 10% to 13% and as L_u^x/c increased from 5 to 10. Increasing freestream Reynolds number by 40% at constant turbulence intensity only resulted in maximum increases of 21% in peak lift coefficient and 25% in peak hinge moment coefficient. Hence, the integral length scales of the approaching eddies with the largest energies and their size relative to the heliostat chord length must be considered for the design of heliostats in the stow position so that they can withstand maximum wind loads during high-wind events.

Lowering the height at which the heliostat is stowed in the simulated ABL from H/δ of 0.5 to 0.3 was found to halve the hinge moment coefficient, despite there being a 10% increase in peak lift coefficient. Additionally, the lowest wind load coefficients were found when the elevation axis height of the heliostat was designed to be half that of the mirror chord length ($H/c = 0.5$). Although heliostats are commonly designed for a minimum H/c of 0.5, larger ratios of H/c are required for heliostats with a horizontal primary axis or for ground clearance if they are cleaned in the normal position. In the current study, reductions of up to 50% in c_L and 40% in $c_{M_{Hy}}$ were found by lowering H/c from 0.7 to 0.5 by manufacturing a heliostat without a horizontal primary axis. This provides the opportunity to lower the critical stow design wind loads for the mirror, drives and support structure, thus lowering the overall mass and strength of the heliostat with a shorter pylon length, and potentially offset the higher capital cost of the drives in a conventional heliostat. The peak lift and peak hinge moment coefficients of the smallest stowed heliostat in the current study were approximately a half and a third, respectively, of those reported by Pfahl et al. (2015) under similar turbulence conditions. These discrepancies may be explained by differences in integral length scales between these studies and the elevation axis height in the ABL (H/δ = 0.3) in the current study that was double that in experiments by Peterka et al. (1989) and Pfahl et al. (2011). The chord length of the heliostat mirrors tested in this study was also found to have a significant influence on the mean and peak wind load coefficients. Reducing the chord length by half of its size resulted in the peak lift coefficient increasing from 0.3 to 0.57 and the peak hinge moment coefficient increasing from 0.05 to 0.09. Therefore, optimisation of the sizes of the mirror chord length and the elevation axis height for the characteristics of the turbulence approaching a stowed heliostat can significantly reduce design wind loads for high-wind events in the atmospheric surface layer. This optimisation can result in significant cost reductions for the manufacturing and installation of the wind-sensitive heliostat components.

Acknowledgements

Support for the work has been provided by the Australian Government Research Training Program Scholarship and by the Australian Solar Thermal Research Initiative (ASTRI) through funding provided by the Australian Renewable Energy Agency (ARENA). The authors would also like to acknowledge the constructive and insightful comments by the anonymous reviewers of the paper.

References

ASCE 7-02, Minimum design loads for buildings and other structures, American Society of Civil Engineers, Reston, Virginia, USA.

Banks, D., 2011, Measuring peak wind loads on solar power assemblies, in: 13th International Conference on Wind Engineering, Amsterdam, Netherlands.

Cook, N.J., 1978, Determination of the model scale factor in wind-tunnel simulations of the adiabatic atmospheric boundary layer, Journal of Wind Engineering and Industrial Aerodynamics 2, 311-321.

Cook, N.J., 1985, The designer's guide to wind loading of building structures, Part 1: Background, damage survey, wind data and structural classification, In: Building Research Establishment, Garston, UK.

Counihan, J., 1973, Simulation of an adiabatic urban boundary layer in a wind tunnel, Atmospheric Environment 7, 673-689.

Coventry, J. and Pye, J., 2014, Heliostat cost reduction–where to now?, Energy Procedia 49, 60-70.

De Bortoli, M., Natalini, B., Paluch, M. and Natalini, M., 2002, Part-depth wind tunnel simulations of the atmospheric boundary layer, Journal of Wind Engineering and Industrial Aerodynamics 90, 281-291.

Emes, M.J., Arjomandi, M., Kelso, R.M. and Ghanadi, F., 2017, Gust characteristics in a low-roughness atmospheric surface layer, Wind and Structures (submitted).

Emes, M.J., Arjomandi, M. and Nathan, G.J., 2015, Effect of heliostat design wind speed on the levelised cost of electricity from concentrating solar thermal power tower plants, Solar Energy 115, 441-451.

ESDU 85020, Characteristics of atmospheric turbulence near the ground - Part II: single point data for strong winds (neutral atmosphere), Engineering Sciences Data Unit, London, UK, 1985.

Farell, C. and Iyengar, A.K., 1999, Experiments on the wind tunnel simulation of atmospheric boundary layers, Journal of Wind Engineering and Industrial Aerodynamics 79, 11-35.

Flay, R.G.J. and Stevenson, D.C., 1988, Integral length scales in strong winds below 20 m, Journal of Wind Engineering and Industrial Aerodynamics 28, 21-30.

Gong, B., Li, Z., Wang, Z. and Wang, Y., 2012, Wind-induced dynamic response of Heliostat, Renewable Energy 38, 206-213.

Gong, B., Wang, Z., Li, Z., Zang, C. and Wu, Z., 2013, Fluctuating wind pressure characteristics of heliostats, Renewable energy 50, 307-316.

Greenway, M.E., 1979, An analytical approach to wind velocity gust factors, Journal of Wind Engineering and Industrial Aerodynamics 5, 61-91.

Hinkley, J.T., Hayward, J.A., Curtin, B., Wonhas, A., Boyd, R., Grima, C., Tadros, A., Hall, R. and Naicker, K., 2013, An analysis of the costs and opportunities for concentrating solar power in Australia, Renewable Energy 57, 653-661.

Holdø, A.E., Houghton, E.L. and Bhinder, F.S., 1982, Some effects due to variations in turbulence integral length scales on the pressure distribution on wind-tunnel models of low-rise buildings, Journal of Wind Engineering and Industrial Aerodynamics 10, 103-115.

Holmes, J.D., Kwok, K.C.S. and Ginger, J.D., 2012, Wind Loading Handbook for Australia and New Zealand: Background to AS/NZS 1170.2 Wind Actions, Australasian Wind Engineering Society, Sydney, Australia.

IRENA, 2013, Renewable Power Generation Costs in 2012: An Overview, Bonn, Germany.

IRENA, 2015, The Power to Change: Solar and Wind Cost Reduction Potential to 2025, Bonn, Germany.

Irwin, H., 1981, The design of spires for wind simulation, Journal of Wind Engineering and Industrial Aerodynamics 7, 361-366.

Jain, A., Jones, N.P. and Scanlan, R.H., 1996, Coupled flutter and buffeting analysis of long-span bridges, Journal of Structural Engineering 122, 716-725.

Kaimal, J.C. and Finnigan, J.J., 1994, Atmospheric Boundary Layer Flows: Their Structure and Measurement, Oxford University Press, New York, USA.

Kolb, G.J., Ho, C.K., Mancini, T.R. and Gary, J.A., 2011, Power tower technology roadmap and cost reduction plan, In: SAND2011-2419, Sandia National Laboratories, Albuquerque, New Mexico, USA.

Kolb, G.J., Jones, S.A., Donnelly, M.W., Gorman, D., Thomas, R., Davenport, R. and Lumia, R., 2007, Heliostat Cost Reduction Study, In: SAND2007-3293, Sandia National Laboratories, Albuquerque, USA.

Kristensen, L., Casanova, M., Courtney, M. and Troen, I., 1991, In search of a gust definition, Boundary-Layer Meteorology 55, 91-107.

Lovegrove, K. and Stein, W., 2012, Concentrating solar power technology: principles, developments and applications, Woodhead Publishing Limited, Cambridge, UK.

Mendis, P., Ngo, T., Haritos, N., Hira, A., Samali, B. and Cheung, J., 2007, Wind loading on tall buildings, EJSE Special Issue: Loading on Structures 3, 41-54.

Milbank, J., Loxton, B., Watkins, S. and Melbourne, W., 2005, Replication of Atmospheric Conditions for the Purpose of Testing MAVs: MAV Flight Environment Project Final Report, Royal Melbourne Institute of Technology.

Nakamura, Y., 1993, Bluff-body aerodynamics and turbulence, Journal of Wind Engineering and Industrial Aerodynamics 49, 65-78.

Peterka, J.A. and Derickson, R.G., 1992, Wind load design methods for ground-based heliostats and parabolic dish collectors, In: SAND92-7009, Sandia National Laboratories, Albuquerque, USA.

Peterka, J.A., Tan, Z., Cermak, J.E. and Bienkiewicz, B., 1989, Mean and peak wind loads on heliostats, Journal of solar energy engineering 111, 158-164.

Pfahl, A., Buselmeier, M. and Zaschke, M., 2011, Wind loads on heliostats and photovoltaic trackers of various aspect ratios, Solar Energy 85, 2185-2201.

Pfahl, A., Randt, M., Meier, F., Zaschke, M., Geurts, C. and Buselmeier, M., 2015, A holistic approach for low cost heliostat fields, Energy Procedia 69, 178-187.

Plate, E.J., 1974, Aerodynamic Characteristics of Atmospheric Boundary Layers, US Atomic Energy Commission, Springfield, Virginia, USA.

Roadman, J.M. and Mohseni, K., 2009, Gust characterization and generation for wind tunnel testing of micro aerial vehicles, AIAA paper 1290, 4166.

AS/NZS 1170.2, Structural Design Actions - Part 2: Wind actions, Standards Australia and Standards New Zealand, Sydney, Australia.

Swamy, N.V.C., Gowda, B.H.L. and Lakshminath, V.R., 1979, Auto-correlation measurements and integral time scales in three-dimensional turbulent boundary layers, Applied Scientific Research 35, 237-249.

Téllez, F., Burisch, M., Villasente, Sánchez, M., Sansom, C., Kirby, P., Turner, P., Caliot, C., Ferriere, A., Bonanos, C.A., Papanicolas, C., Montenon, A., Monterreal, R. and Fernández, J., 2014, State of the Art in Heliostats and Definition of Specifications, In: 609837, STAGE-STE Project, Madrid, Spain.

Watkins, S., 2012, Turbulence Characteristics of the Atmospheric Boundary Layer and Possibilities of Replication for Aircraft, in: Third Symposium "Simulation of Wing and Nacelle Stall", Braunschweig, Germany.